ARTICLES
PUBLISHED ONLINE: 2 OCTOBER 2017 | DOI: 10.1038/NPHYS4279
nature physics

# Probing electronic binding potentials with attosecond photoelectron wavepackets

D. Kiesewetter[1], R. R. Jones[2]*, A. Camper[1], S. B. Schoun[1], P. Agostini[1] and L. F. DiMauro[1]

**The central goal of attosecond science is to visualize, understand and ultimately control electron dynamics in matter over the fastest relevant timescales. To date, numerous schemes have demonstrated exquisite temporal resolution, on the order of ten attoseconds, in measurements of the response of photo-excited electrons to time-delayed probes. However, attributing this response to specific dynamical mechanisms is difficult, requiring guidance from advanced calculations. Here we show that energy transfer between an oscillating field and low-energy attosecond photoelectron wavepackets directly provides coarse-grained information on the effective binding potential from which the electrons are liberated. We employ a dense extreme ultraviolet (XUV) harmonic comb to photoionize He, Ne and Ar atoms and record the electron spectra as a function of the phase of a mid-infrared dressing field. The amplitude and phase of the resulting interference modulations in the electron spectra reveal the average momentum and change in momentum of the electron wavepackets during the first quarter-period of the dressing field after their creation, reflecting the corresponding coarse characteristics of the binding potential.**

Coherent energy transfer from a strong oscillating electric field to (quasi-)free electrons is the basis for much of the physics underlying the response of matter to intense laser fields. Moreover, it provides the clockwork for most attosecond measurements to date[1–17]. According to the simpleman's model[18–20], a free electron which is liberated from its host at time $t=0$ while in the presence of a weak oscillating electric field, $\mathbf{F}(t)=F_\omega(t)\cos(\omega(t-t_0))\hat{\mathbf{z}}$, obtains a momentum boost that is proportional to the vector potential at the instant of its release. (This assumes, without loss of generality, that the vector potential has been defined to be zero at the beginning of the radiation pulse, and the field is sufficiently weak that the electron's energy is much greater than the ponderomotive energy, $U_\mathrm{p}=e^2F_\omega{}^2/4m\omega^2$.) As a result, the release time of the free electron within the oscillating vector potential can be mapped to the change in the electron's momentum (or energy) due to the drive field, making it possible to employ photoelectron spectroscopy to determine relative ejection times with attosecond precision. Specifically, a free electron with initial momentum $p_0$ parallel to the laser field gains an energy

$$W=-\frac{e}{m}p_0\frac{F_\omega}{\omega}\sin(\omega t_0) \qquad (1)$$

from the laser pulse (see Supplementary Information). Here $e$ and $m$ are the electron charge and mass, respectively, and $t_0$ is the time between liberation and the next zero of the vector potential.

This classical ejection time-to-energy encoding also holds for the quantum description of a photoelectron as a wavepacket (see ref. 21 and Supplementary Information). It is exploited in the attosecond 'streaking' technique which was first used to characterize isolated attosecond extreme ultraviolet (XUV) pulses[4,6] via photoionization into a laser-dressed continuum. It has also enabled the exploration of a variety of phenomena occurring on attosecond and femtosecond timescales, including time-resolved photoemission from solids[11], tunnelling times[12], and autoionization[13] or Auger decay[7] in atoms. Of course, invoking the simpleman's direct time-to-energy mapping implicitly assumes a constant momentum $p_0$, ignoring any influence of the parent ion or emitting surface. Therefore, if the mapping is to hold, even approximately, the total energy $E$ of the electrons ejected into the continuum must be much greater than both the binding energy in the electronic ground state, $I_\mathrm{p}$, and the ponderomotive energy of the dressed electron, $U_\mathrm{p}=e^2F_\omega{}^2/4m\omega^2$ (ref. 6).

For ionization near threshold, the streaking concept can still be applied, but the maximum energy transfer and the phase at which this maximum occurs differ substantially from that predicted by equation (1), due to the non-negligible potential, $U(\mathbf{r})$, and the position dependence it imposes on the electron's momentum[22–24]. The measurements described here exploit the failure of the simpleman's model near threshold, allowing us to extract coarse-grained information on the effective binding potential by comparing electron spectra at low and high energies.

Equation (1) describes the effect of a dressing field on an isolated attosecond wavepacket. The same energy-transfer phenomenon underlies reconstruction of attosecond beating by interfering two-photon transitions (RABBITT) measurements[3,25–27]. Our experimental configuration follows the RABBITT prescription, but we extract and use additional information beyond the standard formalism, implementing what we call RABBITT+ to characterize the influence of the binding potential on a coherent train of laser-dressed attosecond photoelectron wavepackets produced by an XUV harmonic comb (see Fig. 1 and Supplementary Information).

RABBITT was originally developed to characterize periodic attosecond pulse trains contained within ionizing XUV harmonic combs. The odd-order harmonics are generated from a replica of the low-frequency dressing field $\mathbf{F}(t)$ (refs 3,25–27). In a RABBITT measurement, the XUV harmonics produce 'direct' photoelectrons at discrete energies. At the same time, the dressing laser coherently redistributes some of the photoelectron amplitude to different energies, forming discrete 'even-order' sidebands between the 'odd-order' direct ionization peaks. The superposition of transition

[1]Department of Physics, The Ohio State University, Columbus, Ohio 43210, USA. [2]Department of Physics, University of Virginia, Charlottesville, Virginia 22904, USA. *e-mail: rrj3c@virginia.edu

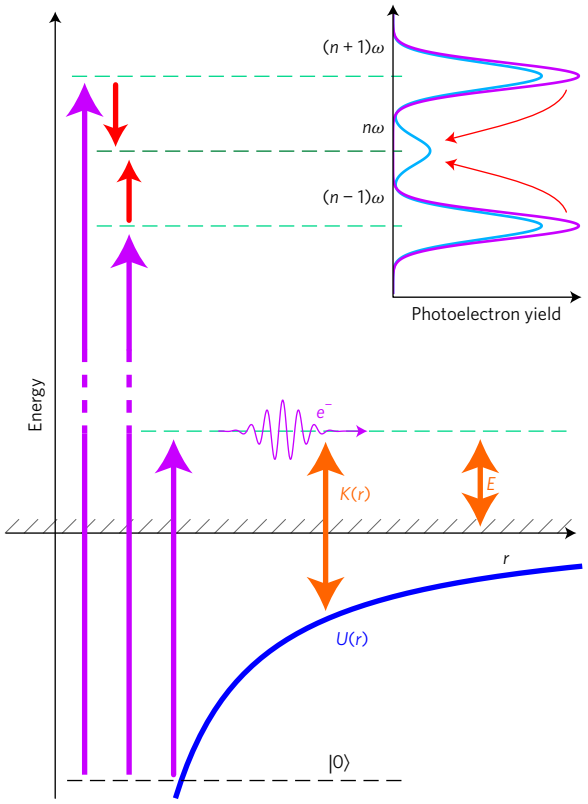


**Figure 1 | Photoionization in a laser-dressed continuum and illustration of the RABBITT+ scheme.** When near its parent ion, a low-energy photoelectron has a kinetic energy $K(r)$ much larger than its total energy $E$, resulting in sidebands which exhibit delay-dependent modulations with a different amplitude and phase than that predicted by the simpleman's model. Purple arrows: XUV (odd-order harmonic) absorption from the ground state $|0\rangle$. Red arrows: absorption and emission of dressing-laser photons from direct, odd-harmonic photoionization channels into even-order sidebands.

amplitudes, from different direct ionization channels into the sidebands, leads to multi-path interference that modulates the amplitude in each sideband as a function of the relative delay, $t_0$, between the ionizing and dressing fields.

Using a semiclassical extension of the simpleman's model (see ref. 28 and Supplementary Information), the delay-dependent yield $P_n$ in the even-order sideband corresponding to the $n$th harmonic is

$$P_n \simeq \frac{e^4}{16m^2\hbar^2}|z_k|^2|\widetilde{f}_{\mathrm{XUV}}|^2\frac{F_\omega^{\,2}}{\omega^4}k_0^{\,2}(1+\beta^2+2\beta\cos(2\omega t_0-\Delta\phi)) \quad (2)$$

where $z_k = \langle \mathbf{k}|z|0\rangle$ is the XUV photoionization dipole matrix element with $\mathbf{k} = \mathbf{p}/\hbar$, $\hbar k_0$ is the electron's momentum along the dressing polarization, $\widetilde{f}_{\mathrm{XUV}}$ is the spectral amplitude of the XUV field in the $(n-1)$th-order harmonic, and $\beta$ and $\Delta\phi$ are the field-amplitude ratio and spectral phase difference, respectively, between the $(n+1)$th and $(n-1)$th harmonics. The sideband yield oscillates at a frequency of $2\omega$ as a function of $t_0$, with an amplitude proportional to the partial kinetic energy, $K_0 = \hbar^2 k_0^{\,2}/2m$. Notably, this amplitude is identically zero at threshold, and the 'atomic phase shift' that appears in RABBITT characterization of XUV pulses in real atoms[3] is absent.

Despite their basis in the driven motion of free electrons, there is great interest in applying streaking and RABBITT as attosecond probes of atomic and molecular processes. For example, both techniques have been employed to measure differences in the times required to photoionize electrons from various orbitals within the same, or different, atomic or molecular species[14,15,29–31], or to identify structure in ionization continua[17,32,33]. However, because ionization 'time delays' and spectral resonances both inherently depend on the binding potentials through which ionized electrons travel, and because those potentials are assumed to be negligible in the basic time-to-energy mapping upon which the measurements rely, the interpretation of such experiments requires substantial theoretical support[24,34–39]. Indeed, the application of attosecond methods to explore electron dynamics in more complex systems has been limited by the lack of a systematic procedure for directly mapping experimental observables to relevant time-dependent properties of the system under study. Here we describe a novel approach to provide one such mapping. Using RABBITT+, we characterize the effective binding potential by measuring sideband amplitudes and atomic phase shifts near threshold, where they are difficult to accurately calculate[37,40], and comparing them to the simpleman's result.

We present an analytic reformulation of field-driven energy transfer, directly relating relevant characteristics of the effective binding potential to our attosecond photoelectron spectroscopy measurements. Experimentally, we implement the RABBITT+ method (described below) with near-threshold photoelectrons which are most sensitive to the binding potential. Specifically, we exploit the fact that in streaking and RABBITT/RABBITT+ measurements, energy transfer to an outgoing electron is principally determined by its average momentum, $\mathcal{P}_1$, during the first quarter-cycle of the dressing field after ejection, and the rate of change, $-\alpha$, in the average momenta, $\mathcal{P}_1$ and $\mathcal{P}_2$ evaluated during the first and second quarter-cycles of the field, respectively. Accordingly, as shown in Fig. 2, RABBITT+ measurements of sideband amplitudes and phases enable the direct evaluation of the atomic phase $2\varphi$ and an effective kinetic energy $\mathcal{K}_0$, which determine $\mathcal{U}_1$, the average effective potential during the interval $0 \le t \le T/4$, as well as the effective force $\alpha$ as the electron moves into the next quarter-cycle. Notably, the effective potential which is probed includes both electron–electron as well as electron–ion interactions.

## Experiment

We recover coarse-grain information ($\mathcal{U}_1$ and $\alpha$) on the effective binding potentials in neon and helium by performing RABBITT+ measurements with low-energy photoelectrons from helium, neon and argon with $I_p = 24.59$, 21.56 and 15.76 eV, respectively. The argon measurements serve as a phase reference for the other two gases. The target atoms are introduced into a magnetic bottle electron spectrometer[41] where they are photoionized by an XUV pulse train, produced via high harmonic generation (HHG) in $CO_2$, in the presence of the dressing field, which is a weak copy of the 1.7 μm HHG driving field ($T/4 = 1.4$ fs). We measure the photoelectron spectrum as function of delay between the XUV and dressing field, producing the RABBITT spectrogram from which we extract sideband yield oscillation amplitudes and phases (see Methods).

With RABBITT+, we measure the net phase, $\Phi = \Delta\phi + 2\varphi$, of the delay-dependent modulations in the yield associated with each even-order photoelectron sideband. When standard RABBITT is applied to characterize an attosecond pulse train, the phase difference $\Delta\phi$ (a function of photon energy that depends only on the XUV properties) is the parameter of interest, whereas $\varphi$ (a function of $E$ that depends only on the binding potential) must be calculated to extract $\Delta\phi$ from $\Phi$ (ref. 3). Here, we seek to measure the near-threshold values of $\varphi$ to recover the coarse characteristics of the electron's time-dependent momentum and, through it, those of the effective binding potential. To do so, we must first determine $\Delta\phi$ at the relevant photon energies. For this, standard RABBITT

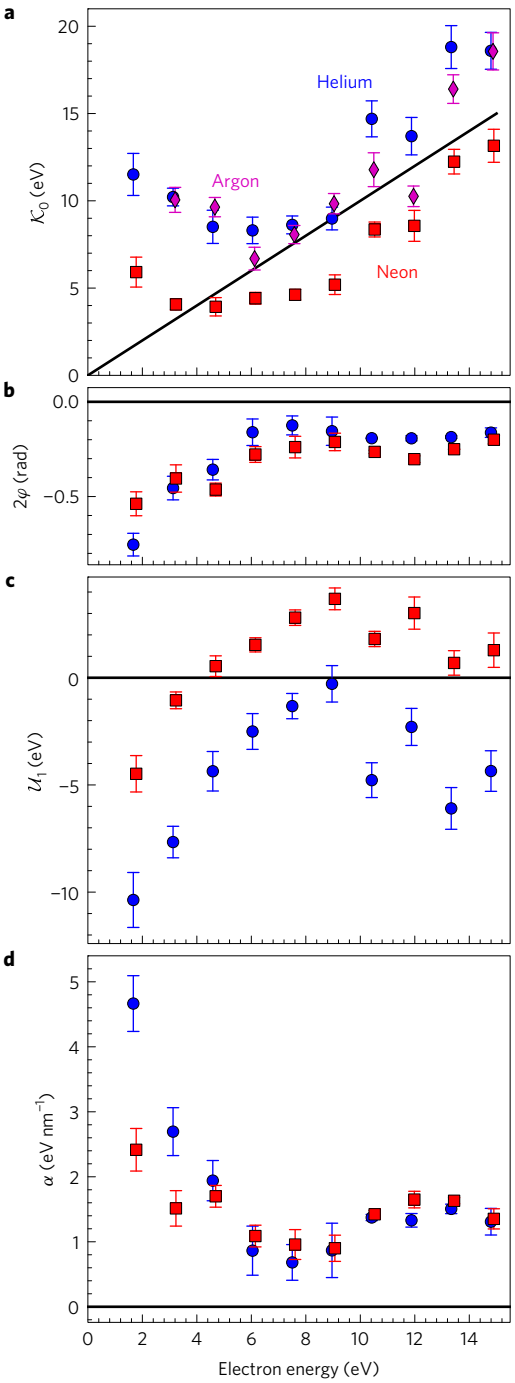


**Figure 2 | Atomic parameters extracted from RABBITT+ measurements.** He (blue circles), Ne (red squares) and Ar (purple diamonds). The thick black line in each plot is the simpleman's prediction for the respective quantity. **a**, Effective kinetic energy, $\mathcal{K}_0$, for each atom. **b**, Atomic phase, $2\varphi$, for each atom. **c**,**d**, $\mathcal{U}_1$ and $\alpha$, respectively, for the effective potential experienced by the departing electron during the first quarter-cycle of the dressing field after its ionization. Both **c** and **d** are derived from the quantities plotted in **a** and **b**. Error bars originate from the standard deviation of multiple measurements (see Methods). The considerable scatter in **a** and **c** for all targets above 10 eV is due to a systematic artefact in the detector collection efficiency which is not reflected in the error bars.

measurements are performed at photoelectron energies above threshold in the low-$I_p$ reference Ar, using established values of $\varphi$ (which are calculable with sufficient accuracy at these energies[37,40]) to determine $\Delta\phi$ for the same harmonics which are relevant to near-threshold photoionization in the higher-$I_p$ targets He and Ne (see Methods and Supplementary Fig. 5).

Extracting binding potential information from RABBITT+ also requires measurement of the sideband amplitudes. The interpretation of the sideband amplitudes and atomic phases are readily understood in the context of the analytic reformulation of electron energy transfer in a coarse-grained pseudo-potential, as motivated and described below.

## Analysis

For a weak dressing-laser pulse, $\mathbf{F}(t)$, with at least several field cycles, the net energy transfer $W$ to a free electron occurs in the time interval between the electron's emission at $t=0$ and the next maxima of the field at $t=t_0$. In a non-zero potential, $W$ is acquired between $t=0$ and the first field maximum after the electron leaves the principal influence of the parent ion[22]. For the near-infrared dressing fields that are commonly used for streaking and RABBITT(+) measurements, even near-threshold photoelectrons exit the binding potential in a fraction of the laser period, allowing us to comfortably define the relevant field maximum as the one that occurs at $T/2+t_0$. Since $W$ is approximately equal to the product of the field and the electron's momentum integrated over roughly the first half-cycle of the field after the electron's emission (see Supplementary Information), and the electron experiences a non-negligible binding potential during only a (small) fraction of this interval, $W$ primarily depends on the average momentum during this time and is, therefore, insensitive to the precise spatial characteristics of $U(\mathbf{r})$. Although this inherently limits the information content in a streaking or RABBITT+ measurement, it allows us to compute the sideband yield in equation (2) (or the energy transfer in equation (1)) using any potential for which the average momentum of the departing electron (during a brief interval after emission) is the same as that in the actual potential.

Accordingly, we employ a one-dimensional pseudo-potential which coarsely describes the dynamics of a photoelectron leaving its parent ion along the dressing-field polarization ($\hat{\mathbf{z}}$), and for which equations (1) and (2) can be readily calculated in terms of the parameters relevant to the actual potential. The pseudo-potential is defined by the average values of the photoelectron momentum $\mathcal{P}_1$ and $\mathcal{P}_2$ in the actual potential, during the time intervals $0\leq t\leq T/4$ and $T/4<t\leq T/2$, respectively (see Fig. 3a). The momentum is allowed to vary linearly in time, with constant slope $-\alpha$ from $0\leq t\leq T/4$, and then assumes a constant value $\mathcal{P}_2$ until some time after the field maxima at $t=T/2+t_0$, the time at which the net energy transfer is complete. The photoelectron energy $E$ and the coarse-grained momentum function determine the relevant pseudo-potential, with $\mathcal{U}_1=E-\mathcal{P}_1^2/2m-(\alpha T/4)^2/24m$ and $\mathcal{U}_2=E-\mathcal{P}_2^2/2m$, the average values of the actual potential during the first quarter-cycle and the following fractional-cycle until the next field maximum, respectively (see Fig. 3b). The energy-dependent pseudo-potential varies linearly with position during the interval, $0\leq t\leq T/4$, with a constant slope $\alpha$. At higher energies the electron travels a greater distance during any quarter-cycle of the field, and spends less time in the deepest part of the actual binding potential. As a result, the coarse-grained momentum function and pseudo-potential approach $p_0$ and zero, respectively, with increasing electron energy.

As outlined in the Supplementary Information, defining the coarse-grained momentum and pseudo-potential parameters on quarter-cycle intervals leads to particularly convenient, analytic expressions for both energy transfer via streaking and RABBITT+ sideband yields. The equations are completely analogous to equations (1) and (2), but with amplitudes and phase shifts that depend explicitly on the coarse characteristics of the effective potential explored by the departing electron while $0\leq t\leq T/4$.

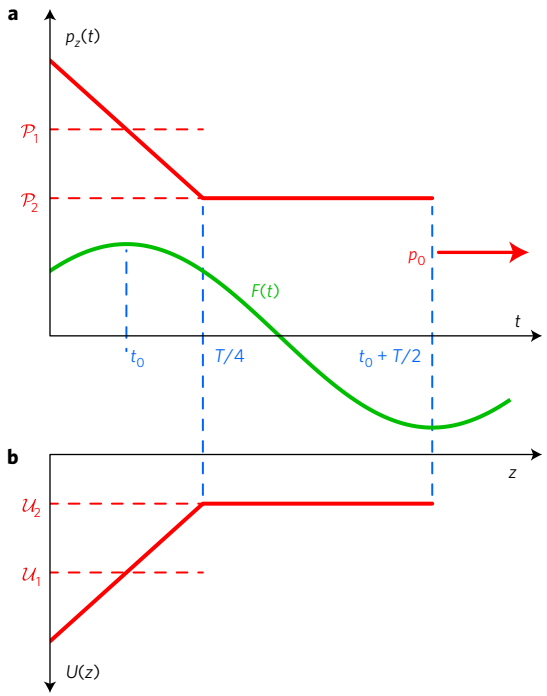


**Figure 3 | Pseudo-potential relevant to energy transfer in a laser-dressed continuum. a**, An electron is ejected at time $t=0$ in the presence of a weak oscillating electric field $F(t)$. For $0 \le t \le T/4$, the electron has an average momentum $\mathcal{P}_1$ and experiences a constant restoring force $\alpha$ along the laser polarization. For $t > T/4$, its momentum is constant at $\mathcal{P}_2$ until after the next field maximum at $T/2+t_0$. Eventually, after the net energy transfer has been established, the electron's momentum assumes its asymptotic value, $p_0$. **b**, Illustration of the corresponding spatial dependence of the pseudo-potential along the field polarization.

For streaking, we find that the central energy of a continuum electron wavepacket is shifted by

$$W \simeq -\frac{e}{m}\mathcal{P}_0\frac{F_\omega}{\omega}\sin(\omega t_0 - \varphi) \tag{3}$$

$$\begin{aligned}\mathcal{P}_0 &= \sqrt{[\mathcal{P}_1 - (1-\pi/4)\alpha/\omega]^2 + (\alpha/\omega)^2} \\ \tan\varphi &= \frac{-\alpha/\omega}{\mathcal{P}_1 - (1-\pi/4)\alpha/\omega}\end{aligned} \tag{4}$$

Although explicitly computed for the pseudo-potential, equations (3) and (4) are valid for any potential for which the departing electron's average momentum takes on the values $\mathcal{P}_1$ and $\mathcal{P}_2$ during the intervals, $0 < t < T/4$ and $T/4 < t < T/2$, respectively. The accuracy of equations (3) and (4) has been confirmed, numerically, for ionization from a variety of potentials and initial binding energies, provided the electron leaves the influence of the potential within the first half-cycle following ionization (see Supplementary Information). As an example, Fig. 4 shows the excellent agreement for a singly charged Coulomb potential, assuming dressing-laser parameters similar to those used in our experiments. For RABBITT(+), a semiclassical analysis can again be used to derive, from equation (3), the yield in the sideband at the $n$th harmonic,

$$\begin{aligned}P_n \simeq\ & \frac{e^4}{16m^2\hbar^4}|z_\kappa|^2|\tilde{f}_{\mathrm{XUV}}|^2\frac{{F_\omega}^2}{\omega^4} \\ & \times {\mathcal{P}_0}^2(1+\beta^2+2\beta\cos(2\omega t_0 - \Delta\phi - 2\varphi))\end{aligned} \tag{5}$$

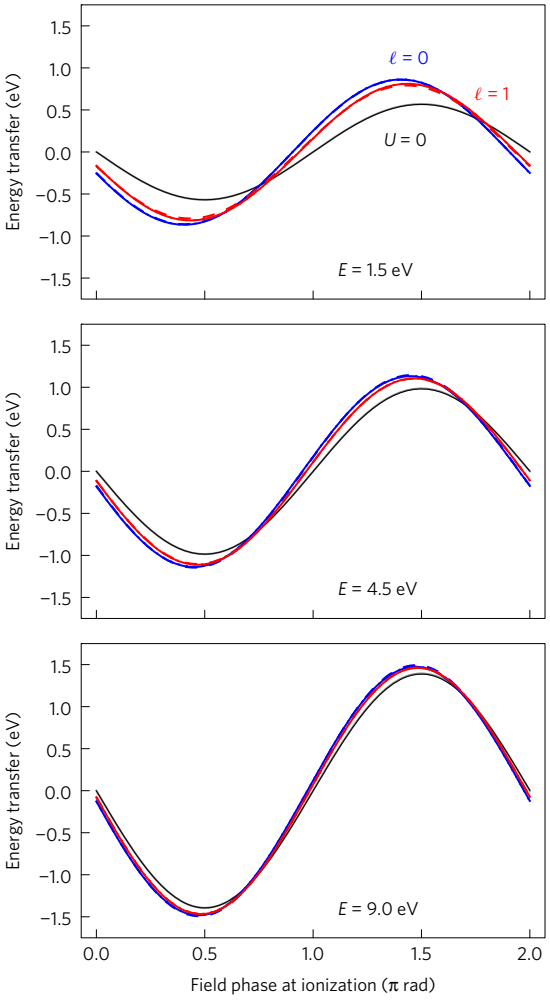


**Figure 4 | Classical energy transfer in laser-dressed Coulomb potentials.** Calculations are performed for a 1.7-μm dressing field with duration 65 fs and peak intensity $10^{11}$ W cm$^{-2}$, for electrons with different $E$ (1.5 eV, 4.5 eV and 9.0 eV for the upper, middle and lower panels, respectively) with no potential (black) and in singly charged effective Coulomb potentials corresponding to two different electron angular momenta: $\ell = 0$ (blue) and $\ell = 1$ (red). The electrons are launched at the most probable radial distance for an electron in the ground state of the respective Coulomb potentials. For each Coulomb potential, solid line: numerical calculation using exact potential; dotted line (hidden behind solid line): fit of equation (3) to the numerical calculation illustrating that equation (3) very accurately captures the functional form of the energy transfer; dashed line: results of equation (3) using the pseudo-potential described in the text with $\mathcal{P}_1$ and $\mathcal{P}_2$ set equal to the average electron momentum in the Coulomb potential during the time intervals $0 \le t \le T/4$ and $T/4 < t \le T/2$, respectively.

where $z_\kappa$ is a dipole matrix element analogous to that in equation (2) but with an altered final state determined by $\boldsymbol{\kappa}(r) = \mathbf{p}(r)/\hbar$, the field-free but position-dependent momentum in the effective potential, with $\kappa(r \to \infty) = k$ (see Supplementary Information).

Equations (3) and (5) are nearly identical to equations (1) and (2), respectively, except that the asymptotic momentum $p_0$ and wavevector $\mathbf{k}$ have been replaced with an effective momentum $\mathcal{P}_0$ and wavevector $\boldsymbol{\kappa}$, and an additional energy-dependent phase factor, $\varphi$ (half of the 'atomic phase'), appears in both equations as a consequence of the non-zero potential. With near-threshold photoelectrons escaping a binding potential, one expects an effective momentum $\mathcal{P}_0$ larger than the asymptotic momentum $p_0$. For ionization far above threshold, where $E \gg \mathcal{U}_1, \mathcal{U}_2$, one can find by

inspection: $\mathcal{P}_1, \mathcal{P}_2 \rightarrow p_0$ and $\alpha \rightarrow 0$. Therefore, for large $E$, $\mathcal{P}_0 \rightarrow p_0$, $\boldsymbol{\kappa} \rightarrow \mathbf{k}$ and $\varphi \rightarrow 0$, recovering the simpleman's result.

Through equation (4), equations (3) and (5) can be used to directly extract coarse-grained information on the time-dependent momentum and effective potential experienced by a dressed photoelectron in a streaking or RABBITT+ experiment. Clearly, it is not sufficient to measure only time delays or phases to obtain this information. One must also record the magnitude of the energy transfer or the delay-averaged sideband yield for streaking or RABBITT+, respectively.

To extract $\mathcal{P}_0$ versus $E$ from the RABBITT+ measurements, we use the undressed yields $P_{n-1}$ and $P_{n+1}$ in adjacent direct ionization peaks to compute the normalized yield $P_n/\sqrt{P_{n-1}P_{n+1}}$ from the oscillating component of the sideband at the $n$th harmonic order. In the absence of resonances, the factors $\widetilde{f}_{\mathrm{XUV}}$ and $z_\kappa$ in equation (5) are only weakly dependent on energy and, given our dense XUV comb, are eliminated through this normalization. Accordingly, the delay-averaged, normalized sideband yield at the energy of the $n$th harmonic is proportional to the effective partial kinetic energy $\mathcal{K}_0 = \mathcal{P}_0^2/2m$, with the constant of proportionality determined by the normalized yields at high energy, as described in Methods.

## Results

The near-threshold values of $\mathcal{K}_0$, representing the effective electron kinetic energies during the first quarter-cycle after ionization, are plotted for Ar, Ne and He in Fig. 2a, along with the simpleman's expectation $\mathcal{K}_0 = E$. The results for Ar and He are roughly as expected, with $\mathcal{K}_0$ considerably larger than $E$ at low energies, becoming only slightly larger or comparable to $E$ with increasing energy. The result for Ne is more interesting, with $\mathcal{K}_0 < E$ at all but the lowest energies, not indicative of a purely attractive effective binding potential. Naively, one might expect a greater similarity between the Ar and Ne results (as opposed to Ar and He) given the different initial and final angular momentum channels in He.

The near-threshold atomic phases which are extracted for He and Ne are plotted in Fig. 2b. Qualitatively, the results have the expected deviation from the simpleman's model. The small values of $\varphi$ at high energy, where the effective potential has little influence on the energy transfer, rapidly increase in magnitude approaching threshold, where the potential dominates the energy transfer.

Following equation (4), the experimentally determined values of $\mathcal{P}_0$ and $\varphi$ define the average momentum, and rate of change in momentum, of the departing photoelectron during the first quarter-cycle of the dressing field following ionization. In turn, these quantities can be used to obtain $\mathcal{U}_1$ and $\alpha$, which reflect the average potential (see Fig. 2c) and change in potential (see Fig. 2d) during this 1.4 fs time interval. In addition, the quantity $\mathcal{U}_1 T/4\hbar$ represents the net phase shift of the photoelectron wavepacket, after it has travelled for a time $T/4$ through the most significant part of the binding potential, relative to that of a free electron with the same total energy.

In He, the effective potential agrees qualitatively with expectations. Both $\mathcal{U}_1$ and $\alpha$ are the most pronounced at low $E$, where the effect of the non-zero binding potential is most prominent. As $E$ increases, the electron spends less time in the deepest and steepest part of the potential, reducing the depth and slope of the potential when averaged over the quarter-cycle (1.4 fs) time interval. The effective potential for Ne is distinctly different. First, it has a relatively modest average gradient, even very near threshold. Second, the magnitude of $\mathcal{U}_1$ is only a few eV at most and actually changes sign for $E > 4$ eV. One interpretation of this result is that the physical potential has a repulsive component that dominates the energy transfer at rather large distances from the atom. However, it is important to remember that the methods we employ provide information on the effective potential, including multi-electron interactions.

The data are qualitatively consistent with previous theoretical results. Namely, the RABBITT+ sideband amplitudes in He (Ne) calculated by Mauritsson *et al.*[40] are consistently higher (lower) than predicted by the simpleman's model, suggesting that the effective momentum of the photoelectron ejected from the two atoms is greater (less) than $p_0$. Supplementary Fig. 6 shows the result of applying our analysis to directly extract coarse-grained information on the electron momentum and the effective potential from the sideband amplitudes and phases computed by Mauritsson and colleagues[40]. Although there are quantitative differences in calculated and measured parameters, there are key similarities as well, including a considerably larger magnitude of $\mathcal{U}_1$ in He relative to Ne, a greater value of $\alpha$ at low energy in He as compared to Ne, and the curious change in sign of $\mathcal{U}_1$ with increasing energy in Ne. The distinctions between the coarse characteristics of the effective potentials in Ne and He suggest real differences in the influence that other electrons have on the departing electron in these atoms.

## Conclusion

Beyond the atomic systems studied here, the RABBITT+ technique should also be applicable to molecules. Although ionization into excited ionic states and dissociation present additional technical challenges, RABBITT measurements in molecules have already been reported[31], and extensions to RABBITT+ should be possible. Also, although we have not shown it here due to insufficient signal to noise, in principle, finer details of the long-range part of the actual potential may be accessible by comparing the changes in the coarse characteristics of the potential as a function of electron energy. Moreover, applying our method to streaking experiments should enable the direct measurement of changes in the effective potential experienced by a departing electron due to additional atomic or molecular ionization, or ultrafast structural rearrangement.

## Methods

Methods, including statements of data availability and any associated accession codes and references, are available in the online version of this paper.

Received 22 May 2017; accepted 31 August 2017; published online 2 October 2017

## References


1. Corkum, P. B. & Krausz, F. Attosecond science. *Nat. Phys.* **3,** 381–387 (2007).
2. Krausz, F. & Ivanov, M. Attosecond physics. *Rev. Mod. Phys.* **81,** 163–234 (2009).
3. Paul, P. M. *et al*. Observation of a train of attosecond pulses from high harmonic generation. *Science* **292,** 1689–1692 (2001).
4. Hentschel, M. *et al*. Attosecond metrology. *Nature* **414,** 509–513 (2001).
5. Niikura, H. *et al*. Sub-laser-cycle electron pulses for probing molecular dynamics. *Nature* **417,** 917–922 (2002).
6. Kienberger, R. *et al*. Steering attosecond electron wave packets with light. *Science* **297,** 1144–1148 (2002).
7. Drescher, M. *et al*. Time-resolved atomic inner-shell spectroscopy. *Nature* **419,** 803–807 (2002).
8. Goulielmakis, E. *et al*. Direct measurement of light waves. *Science* **305,** 1267–1269 (2004).
9. Johnsson, P. *et al*. Attosecond electron wave packet dynamics in strong laser fields. *Phys. Rev. Lett.* **95,** 013001 (2005).
10. Baker, S. *et al*. Probing proton dynamics in molecules on an attosecond time scale. *Science* **312,** 424–427 (2006).
11. Cavalieri, A. L. *et al*. Attosecond spectroscopy in condensed matter. *Nature* **449,** 1029–1032 (2007).
12. Eckle, P. *et al*. Attosecond ionization and tunneling delay time measurements in helium. *Science* **322,** 1525–1529 (2008).
13. Wang, H. *et al*. Attosecond time-resolved autoionization of argon. *Phys. Rev. Lett.* **105,** 143002 (2010).
14. Schultze, M. *et al*. Delay in photoemission. *Science* **328,** 1658–1662 (2010).
15. Klünder, K. *et al*. Probing single-photon ionization on the attosecond time scale. *Phys. Rev. Lett.* **106,** 143002 (2011).

16. Niikura, H., Wörner, H. J., Villeneuve, D. M. & Corkum, P. B. Probing the spatial structure of a molecular attosecond electron wave packet using shaped recollision trajectories. *Phys. Rev. Lett.* **107,** 093004 (2011).
17. Gruson, V. *et al*. Attosecond dynamics through a fano resonance: monitoring the birth of a photoelectron. *Science* **354,** 734–738 (2016).
18. van Linden van den Heuvell, H. B. & Muller, H. G. Limiting cases of excess-photon ionization. in *Multiphoton Processes: Proc. 4th Int. Conf. Multiphoton Processes* (eds Smith, S. & Knight, P.) 25–34 (Cambridge Univ. Press, 1988).
19. Gallagher, T. F. Above-threshold ionization in low-frequency limit. *Phys. Rev. Lett.* **61,** 2304–2307 (1988).
20. Corkum, P. B., Burnett, N. H. & Brunel, F. Above-threshold ionization in the long-wavelength limit. *Phys. Rev. Lett.* **62,** 1259–1262 (1989).
21. Su, J., Ni, H., Becker, A. & Jaroń-Becker, A. Attosecond-streaking time delays: finite-range property and comparison of classical and quantum approaches. *Phys. Rev. A* **89,** 013404 (2014).
22. Shuman, E. S., Jones, R. R. & Gallagher, T. F. Multiphoton assisted recombination. *Phys. Rev. Lett.* **101,** 263001 (2008).
23. Overstreet, K. R., Jones, R. R. & Gallagher, T. F. Phase-dependent electron–ion recombination in a microwave field. *Phys. Rev. Lett.* **106,** 033002 (2011).
24. Zhang, C.-H. & Thumm, U. Electron–ion interaction effects in attosecond time-resolved photoelectron spectra. *Phys. Rev. A* **82,** 043405 (2010).
25. Véniard, V., Taïeb, R. & Maquet, A. Phase dependence of $(n+1)$-color $(n>1)$ IR–UV photoionization of atoms with higher harmonics. *Phys. Rev. A* **54,** 721–728 (1996).
26. Muller, H. G. Reconstruction of attosecond harmonic beating by interference of two-photon transitions. *Appl. Phys. B* **74,** s17–s21 (2002).
27. Mairesse, Y. *et al*. Attosecond synchronization of high-harmonic soft x-rays. *Science* **302,** 1540–1543 (2003).
28. Muller, H. G., van Linden van den Heuvell, H. B. & van der Wiel, M. J. Dressing of continuum states after MPI of Xe in a two-colour experiment. *J. Phys. B* **19,** L733–L739 (1986).
29. Guénot, D. *et al*. Measurements of relative photoemission time delays in noble gas atoms. *J. Phys. B* **47,** 245602 (2014).
30. Sabbar, M. *et al*. Resonance effects in photoemission time delays. *Phys. Rev. Lett.* **115,** 133001 (2015).
31. Huppert, M., Jordan, I., Baykusheva, D., von Conta, A. & Wörner, H. J. Attosecond delays in molecular photoionization. *Phys. Rev. Lett.* **117,** 093001 (2016).
32. Palatchi, C. *et al*. Atomic delay in helium, neon, argon and krypton. *J. Phys. B* **47,** 245003 (2014).
33. Schoun, S. B. *et al*. Attosecond pulse shaping around a Cooper minimum. *Phys. Rev. Lett.* **112,** 153001 (2014).
34. Pazourek, R., Nagele, S. & Burgdörfer, J. Attosecond chronoscopy of photoemission. *Rev. Mod. Phys.* **87,** 765–802 (2015).
35. Ivanov, M. & Smirnova, O. How accurate is the attosecond streak camera? *Phys. Rev. Lett.* **107,** 213605 (2011).
36. Nagele, S. *et al*. Time-resolved photoemission by attosecond streaking: extraction of time information. *J. Phys. B* **44,** 081001 (2011).
37. Dahlström, J. M., L'Huillier, A. & Maquet, A. Introduction to attosecond delays in photoionization. *J. Phys. B* **45,** 183001 (2012).
38. Su, J., Ni, H., Becker, A. & Jaroń-Becker, A. Numerical simulation of time delays in light-induced ionization. *Phys. Rev. A* **87,** 033420 (2013).
39. Kheifets, A. S., Bray, A. W. & Bray, I. Attosecond time delay in photoemission and electron scattering near threshold. *Phys. Rev. Lett.* **117,** 143202 (2016).
40. Mauritsson, J., Gaarde, M. B. & Schafer, K. J. Accessing properties of electron wave packets generated by attosecond pulse trains through time-dependent calculations. *Phys. Rev. A* **72,** 013401 (2005).
41. Kruit, P. & Read, F. H. Magnetic field paralleliser for $2\pi$ electron-spectrometer and electron-image magnifier. *J. Phys. E* **16,** 313–324 (1983).

## Acknowledgements

L.F.D. was supported by the US Department of Energy, Office of Science, Basic Energy Sciences, under Award #DE-FG02-04ER15614. R.R.J. was supported by the US Department of Energy, Office of Science, Basic Energy Sciences, under Awards #DE-FG02-00ER15053 (initial measurements and theory) and #DE-SC0012462 (analysis and manuscript preparation).

## Author contributions

D.K. performed the measurements, reduced the experimental data, and developed/performed the analysis and numerical simulations. R.R.J. conceived the experiments and analytical approach, provided guidance during the data analysis, and assisted with the initial measurements. S.B.S. and A.C. assisted with the experimental set-up and data collection. L.F.D. and P.A. provided key insights and supervision during the experiments and analysis. D.K., R.R.J. and L.F.D. prepared the manuscript, which was discussed among all authors.

## Additional information

Supplementary information is available in the online version of the paper. Reprints and permissions information is available online at www.nature.com/reprints. Publisher's note: Springer Nature remains neutral with regard to jurisdictional claims in published maps and institutional affiliations. Correspondence and requests for materials should be addressed to R.R.J.

## Competing financial interests

The authors declare no competing financial interests.

## Methods

**Experiment.** We use 65 fs (full-width at half-maximum intensity), 1.7 μm ($\hbar\omega = 0.73$ eV, $T/4 = 1.4$ fs), 2 mJ laser pulses which serve as the fundamental for the HHG process and the dressing field. The laser pulses are derived from an optical parametric amplifier pumped by the 800 nm output of a 1 kHz Ti:sapphire amplifier. We choose 1.7 μm for the fundamental wavelength to provide a denser energy sampling by the XUV comb, and because the resulting photoelectron energies are nearly identical in all three gases, allowing for direct comparison of electron spectra without a precise calibration of the energy-dependent detection efficiency. $CO_2$ is used as the generation gas due to its low $I_p$ and structure-free HHG in the energy range studied. Low-energy photoelectrons were collected with the assistance of an accelerating potential in the spectrometer flight tube.

The RABBITT+ experiments involve, in addition to the usual determination of the phases of the sideband modulations, the measurement of populations in both the odd-order harmonic and sideband channels. Odd-order harmonic populations are determined from the maximum value of the harmonic peaks in the dressing-free reference spectrum. Sideband populations are determined from the maxima in the $2\omega$ component of the fast Fourier transform of the RABBITT+ delay scan. Similar results are obtained by integrating the yields over the respective spectral features, except in energy regions where the peaks begin to overlap due to limited spectrometer resolution. The $2\omega$ component phase, $\Phi$, is determined by first integrating over each harmonic, then taking the fast Fourier transform.

Five data sets are combined to produce the results shown in Fig. 2. Each data set includes two RABBITT+ measurements for each target atom, and a dressing-free reference spectrum is collected before and after each RABBITT+ scan. The latter is used to retrieve the odd-harmonic amplitudes and account for slow drifts of the laser system. The intensity of the dressing field is higher than that for typical RABBITT measurements, as required to improve statistics against the unfavourable energy scaling of the sideband yields at low energy. The higher intensity results in a measurable $4\omega$ oscillation component of up to 30% of the $2\omega$ oscillations, but only at the highest energies shown in Supplementary Fig. 4, and in only some of the data sets. Based on the amplitude ratio of the $4\omega$ and $2\omega$ components, we estimate the dressing intensity to range between 1.1 and $3.1 \times 10^{10}$ W cm$^{-2}$.

**Analysis.** As noted above, five data sets (each containing multiple RABBITT+ measurements for each target) are combined to produce the results shown in Fig. 2. Although we can ensure that the dressing-laser intensity is very nearly constant for different targets in the same data set, small differences in the effective dressing-laser intensity for different data sets are unavoidable, due primarily to small variations in the spatial overlap of the XUV and dressing-laser beams. Within the same target species, these intensity variations result in proportional, systematic differences in the sideband yields from data set to data set (see equation (5)). Accordingly, prior to combining the different data sets to obtain the average sideband yields for each target, we first correct for the small intensity variations. For each data set, a single multiplicative factor is used to rescale all the yields so that they best match the respective values from every other data set. Once the data sets for each target are combined, the average high-energy asymptotic behaviour defines the single, global scaling factor that we use to convert normalized sideband yield to $\mathcal{P}_0$ or $\mathcal{K}_0$. This process preserves the (small) relative differences between targets in the normalized yields at the highest electron energies available in the experiments.

Atomic phase variations, due to Ar continuum resonances, are not taken into account in the computed values of $\varphi_{Ar}$ we have used to extract $\Delta\phi$ for the harmonics relevant to near-threshold photoionization in He and Ne[40]. As described in the Supplementary Information, the effects of these resonances are removed from the Ar phase measurements by slightly altering the fundamental wavelength, detuning the harmonics from these resonances.

Due to the considerable variation in $\varphi_{Ar}$ across the broad Cooper minimum[42] that is centred near $E = 35$ eV (but whose effects on the sideband amplitudes and phases extend downward to approximately 25 eV) (ref. 33), we restrict our phase measurement to XUV photon energies $<40$ eV. In principle, the near-threshold ($E < 15$ eV) atomic phases for He and Ne can then be trivially obtained from the measured values of $\Phi$ for each sideband. However, since the RABBITT+ interferometer is not actively stabilized, the relative delay between the XUV and dressing pulses varies between measurements. As a result, there is an additional, unknown offset phase for each target gas. We eliminate this offset phase by defining the atomic phase for each species, at an energy well above threshold (45 eV photon energy), to be equal to its (small) calculated value[40]. Similar overall results are obtained if the extracted atomic phases are, instead, referenced to their calculated values at a 37 eV reference photon energy (below the Cooper minimum in argon). The continuum–continuum part of the total atomic phase calculated in ref. 40 has been adjusted to match the experimental wavelength using an analytical approximation of the continuum–continuum phase[37]. This enables us to define $\varphi_{Ne}(E = 23.7\,\text{eV}) = 0.033$ and $\varphi_{He}(E = 20.6\,\text{eV}) = 0.038$.

**Data availability.** The data that support the plots within this paper and other findings of this study are available from the corresponding author upon reasonable request.

## References

42. Cooper, J. W. Photoionization from outer atomic subshells. A model study. *Phys. Rev.* **128,** 681–693 (1962).